

## Supplementary Information for

### Linking Far-from-Equilibrium Defect Structures in Ceramics to Electromagnetic Driving Forces

Nathan Nakamura<sup>a</sup>, Laisuo Su<sup>a</sup>, Han Wang<sup>b</sup>, Noam Bernstein<sup>c</sup>, Shikhar Jha<sup>a</sup>, Elizabeth Culbertson<sup>d</sup>, Haiyan Wang<sup>b</sup>, Simon J. L. Billinge<sup>d, e</sup>, C. Stephen Hellberg<sup>c</sup>, and B. Reeja Jayan<sup>a</sup>  
Correspondence to: [bjayan@andrew.cmu.edu](mailto:bjayan@andrew.cmu.edu)

## S1. Supplementary Figures and Tables – Materials and Methods

### S1.1 PDF Data Collection and Analysis

*Table S1: PDF measurement standards and experimental resolution from standard refinements*

Detector Distance (mm)	Wavelength (Å)	Standard	$Q_{\text{damp}}$ (Å <sup>2</sup> )	$Q_{\text{broad}}$ (Å <sup>2</sup> )
204.162	0.184769	Ni	0.0384	0.0142

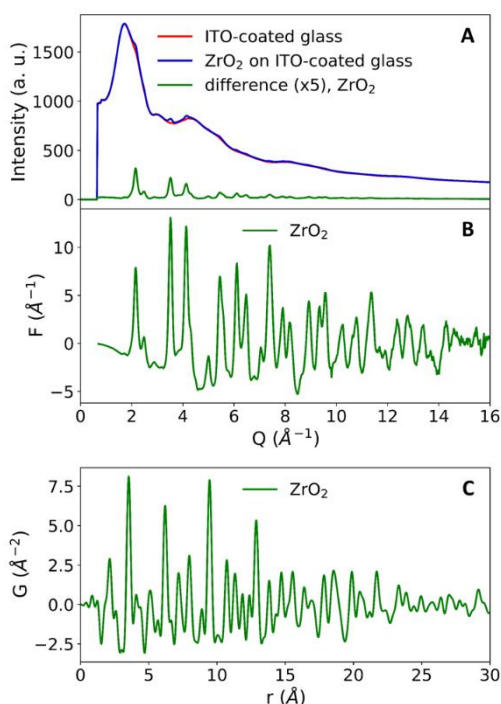


**Fig. S1 Background subtraction and PDF generation from 2D diffraction intensities.** (a) Background subtraction of the scattering intensity of the glass/ITO substrate (red) from  $I(Q)$  for a ZrO<sub>2</sub> MWR-grown film (blue). The difference is shown offset below in green (magnified x5) and corresponds to only the scattering signal left from the ZrO<sub>2</sub> film. (b) The reduced scattering total structure function,  $F(Q)$ . (c) The resultant experimental PDF,  $G(r)$ .

Grain sizes ( $D_c$ ) during PDF analysis are assumed to be spherical, and the calculated model PDF is multiplied by a function  $G_{sphere}$  to account for this.  $G_{sphere}$  is given by

$$G_{sphere}(r, D_c) = \left[ 1 - \frac{3r}{2D_c} + \frac{1}{2} \left( \frac{r}{D_c} \right)^3 \right] H(D_c - r)$$

Where  $D_c$  is the grain size and  $H$  is a step function which equals 1 for  $r \leq D_c$  and 0 beyond. When PDF peaks dampen to zero before the instrumental dampening, the  $r$  value at which peak intensities become zero gives a direct measurement of the average grain size. In our experiments, the instrumental dampening provides resolution out to 75-80 Å, larger than the predicted grain size of the MWR-grown ZrO<sub>2</sub>. This is demonstrated by the decay in PDF peak intensity observed from a crystalline Ni standard, in which peaks correlating to the Ni structure exist out to approximately 80 Å (Fig. S2).

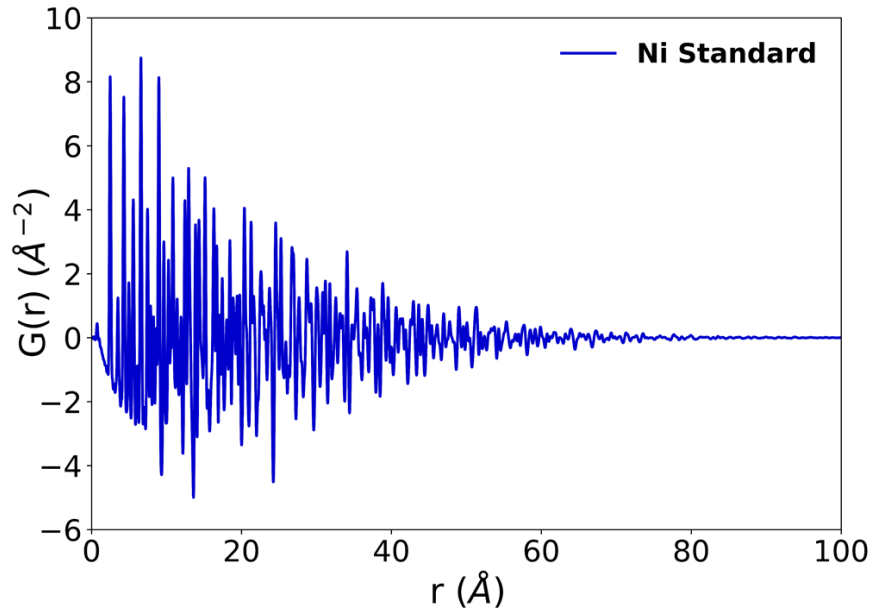


**Fig. S2 Ni PDF data and instrumental dampening.** The Ni PDF data demonstrates that instrumental dampening leads to peak intensities reaching zero around 80 Å in a perfectly crystalline material. Thus, any additional dampening observed in MWR-grown ZrO<sub>2</sub> is due to the finite size of the scattering domains and can be accurately related back to the grain size.

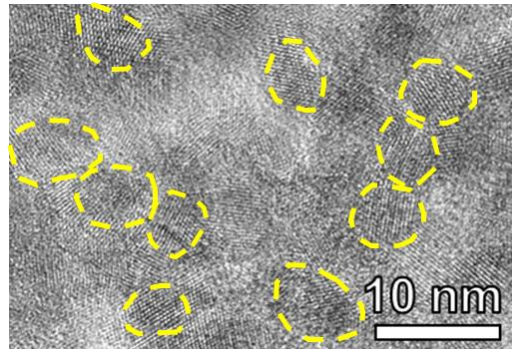


**Fig. S3 TEM of MWR-grown ZrO<sub>2</sub>.** Transmission electron microscopy (TEM) image of the nanocrystalline MWR-grown ZrO<sub>2</sub> thin film (select grains outlined in yellow). The grain sizes observed in the TEM image align with the  $D_c$  values found during PDF fitting.

## S1.2 EXAFS Data Collection and Analysis

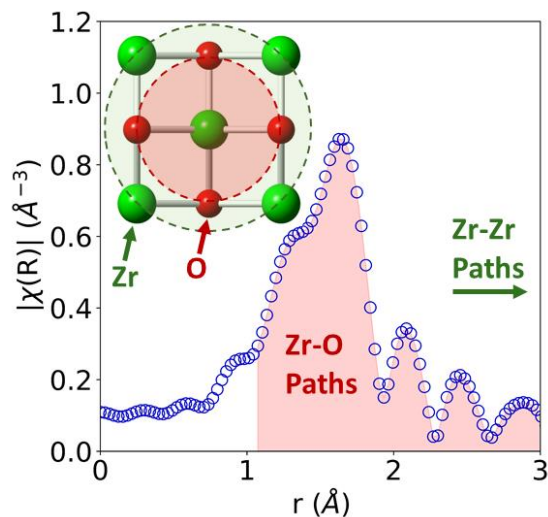


**Fig. S4 EXAFS data interpretation.** EXAFS provides structural information around a central absorber atom within a few coordination shells. Peaks in the EXAFS are related to interatomic distances by the scattering path of the ejected photoelectron during the absorption process. Zr-O paths are indicated in red, along with the corresponding coordination shell in the tetragonal  $\text{ZrO}_2$  structure.

## S1.3 *In-Situ* Microwave Cyclic Voltammetry

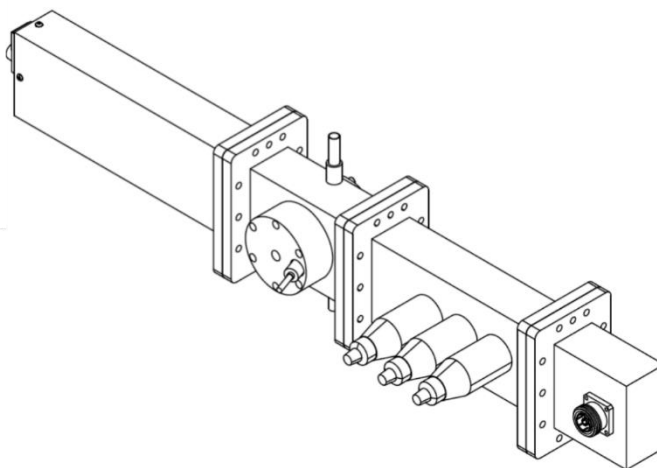


**Fig. S5 Custom-built microwave waveguide used for *in-situ* MW-CV experiments.** Schematic of the waveguide used for *in-situ* MW-CV experiments. MWR was supplied to the waveguide via a coaxial cable connected to an SG 1024 solid state microwave generator (MKS Instruments).

## S2. Supplementary Figures and Tables – Results and Discussion

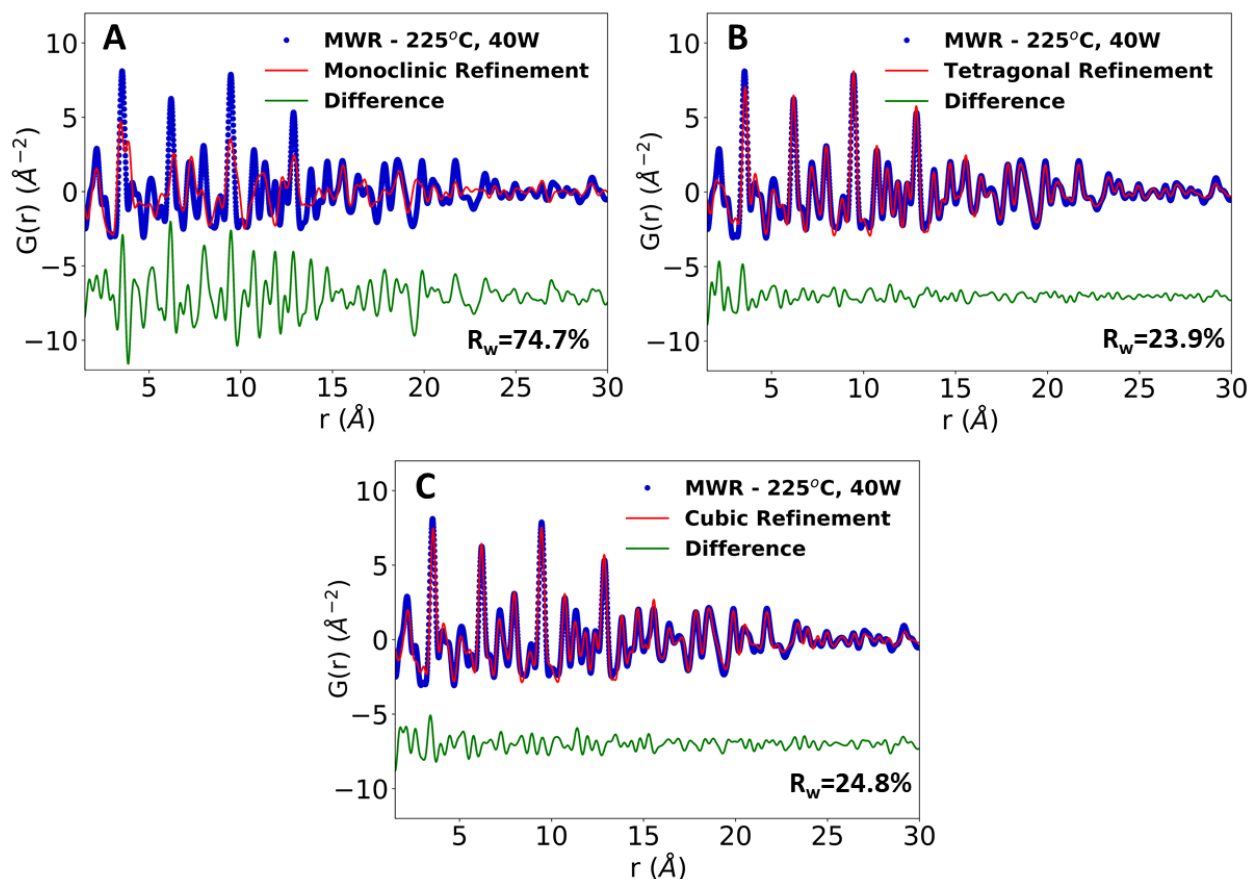


**Fig. S6 Full  $r$ -range PDF refinements to common crystalline phases of  $\text{ZrO}_2$ .** PDF data (blue) for an MWR-grown  $\text{ZrO}_2$  film at 225°C, 40 W to various  $\text{ZrO}_2$  phases (red). Fits are carried out for the monoclinic (a), tetragonal (b), and cubic (c) phases, with tetragonal having the lowest  $R_w$  value. Refinement details are given in Table S3.

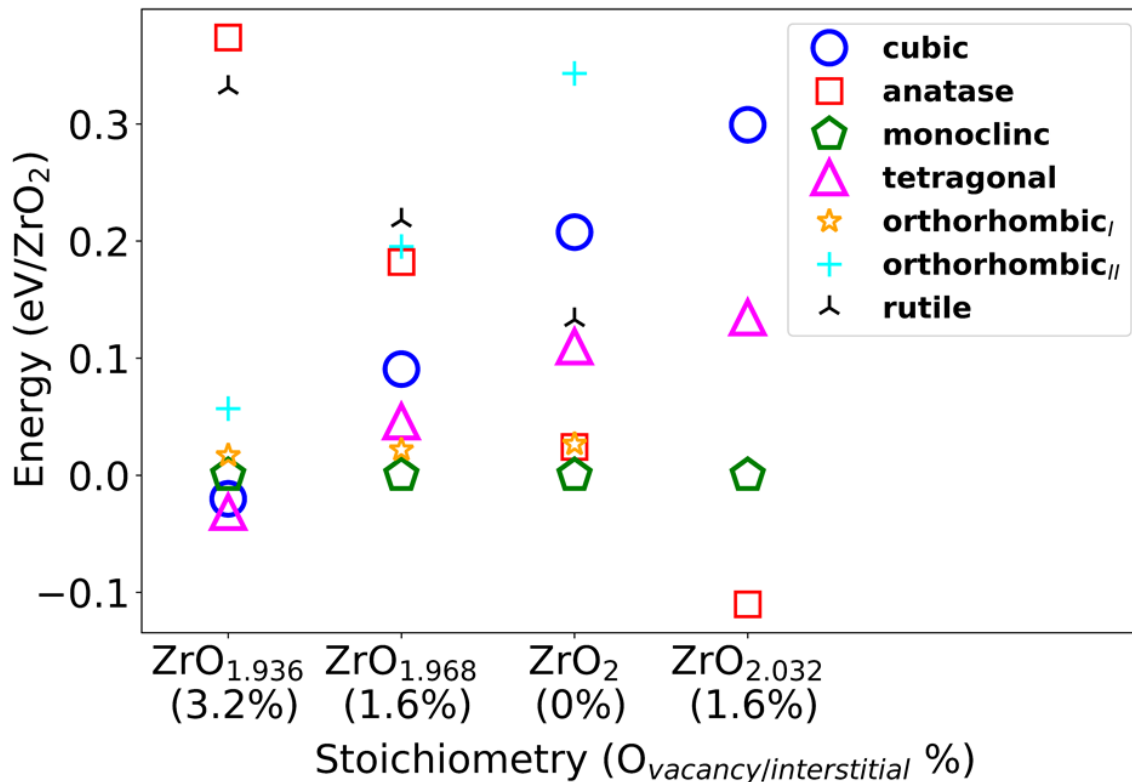


**Fig. S7 Predicted DFT energy vs stoichiometry for various ZrO<sub>2</sub> polymorphs.** DFT energy vs stoichiometry for various ZrO<sub>2</sub> phases, with energies shown relative to the monoclinic phase. At high vacancy concentrations, a defective tetragonal phase becomes the most energetically stable.

**Table S2: DFT-predicted energy, relative to monoclinic**

	ZrO <sub>1.936</sub> (3.2%)	ZrO <sub>1.968</sub> (1.6%)	ZrO <sub>2</sub> (0%)	ZrO <sub>2.032</sub> (1.6%)
<b>Monoclinic</b>	0.0	0.0	0.0	0.0
<b>Anatase</b>	0.3739052	0.1821519	0.0241714	-0.1102738
<b>Cubic</b>	-0.0200721	0.0907059	0.2076641	0.2993408
<b>Tetragonal</b>	-0.0315285	0.0459109	0.1098730	0.1346849
<b>Orthorhombic I</b>	0.0168829	0.0217262	0.0266020	N/A
<b>Orthorhombic II</b>	0.0569422	0.1954468	0.3432267	N/A
<b>Rutile</b>	0.3311763	0.2179026	0.1328730	N/A

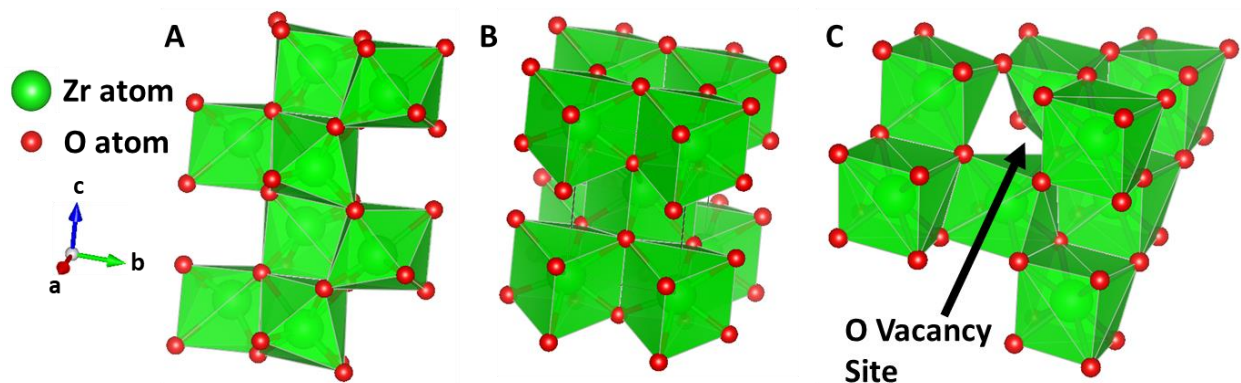


**Fig. S8 Comparison of the monoclinic, tetragonal, and defective tetragonal crystal structures.** Zr atoms are shown in green, with O atoms in red. (a) The monoclinic crystal structure, showing 7-fold coordination. (b) The tetragonal structure, with 8 O atoms around each Zr atom. (c) The defective tetragonal model. Zr atoms are predominantly 8-fold coordinated, with certain Zr atoms surrounded by only 7 O atoms due to the defect. The location of the O vacancy is denoted by the arrow in (c). The defective tetragonal structure consists of edge sharing polyhedra resembling distorted cubes, similar to the defect-free tetragonal phase. However, the distortion in defect-free tetragonal is an elongation along the c-axis, leading to a symmetric distribution of nearest neighbor distances. In the defective structure, this distortion is impacted by relaxations around the vacancy which break the local symmetry (Fig. S9).

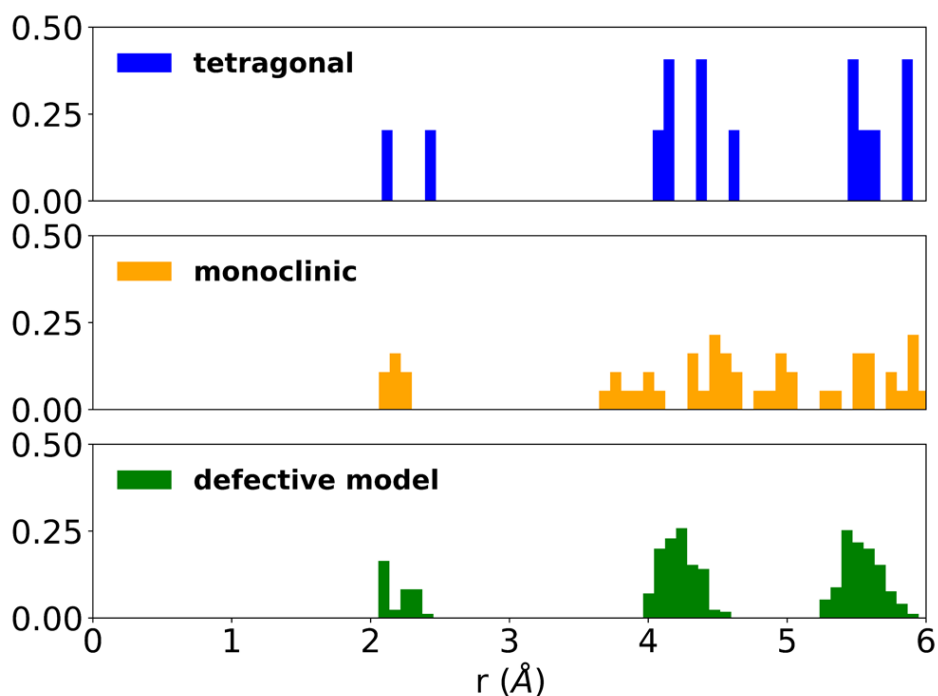


**Fig. S9 Histogram of Zr-O interatomic distances in the tetragonal phase, monoclinic phase, and defective model.** Zr-O bond distances in the tetragonal, monoclinic, and defective phases indicate that the local structural distortions in the defect model lead to an interatomic distance distribution that is no longer tetragonal, but maintains higher symmetry than the monoclinic phase.

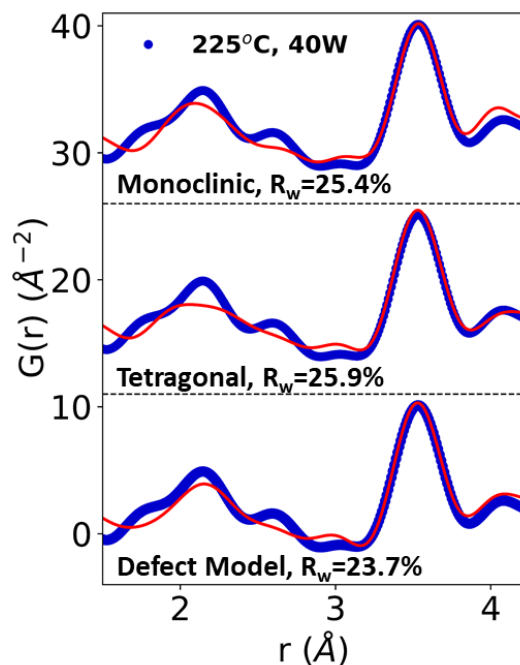


**Fig. S10 PDF refinements to nearest neighbor distances in MWR-grown  $\text{ZrO}_2$ .** PDF data (blue) fit over an  $r$ -range of 1.5-4.2 Å. Refinements are shown in red to the monoclinic (top), tetragonal (middle), and the defective tetragonal phase (bottom). The local atomic order is best described by the local distortions present in the defective model. Refinement details are given in Table S3.

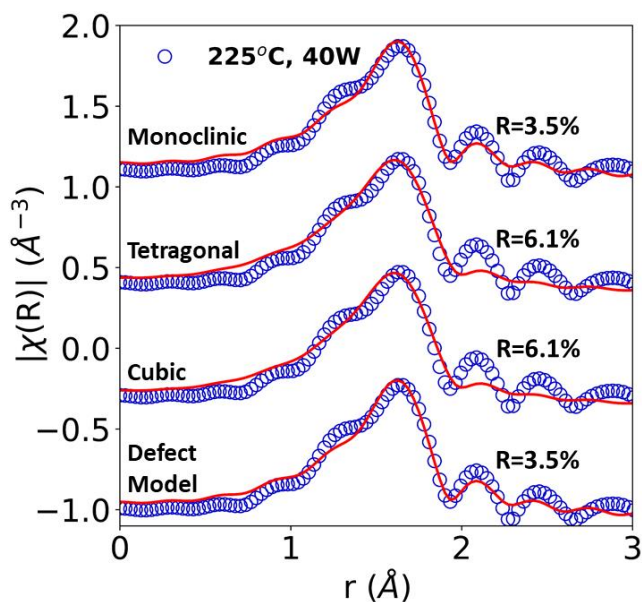


**Fig. S11 EXAFS fitting results for various  $\text{ZrO}_2$  phases.** EXAFS data for a 225°C, 40W MWR-grown  $\text{ZrO}_2$  thin film, fit to different phases. The monoclinic and defective tetragonal model better describe the local Zr-O coordination environment relative to the tetragonal and cubic phases. The defect model provides the most suitable depiction of the local structure based on refined parameter values (Table S4).

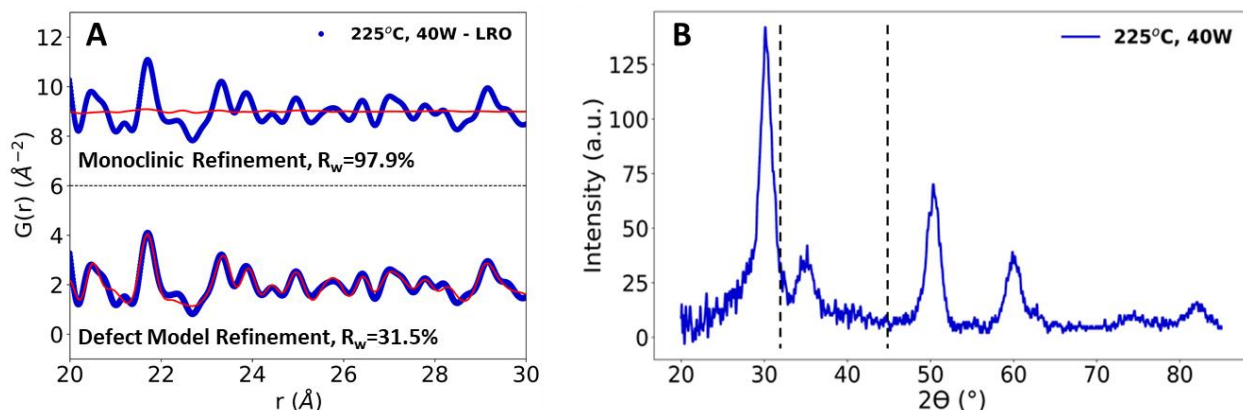


**Fig. S12 Long-range order of MWR-grown  $\text{ZrO}_2$ .** (a) PDF data (blue) fit in the LRO regime to the monoclinic phase (top) and defective model (bottom). The lack of any peaks in the fit monoclinic phase indicate that no monoclinic LRO is present. (b) XRD data from the same thin film indicated in (a). All visible Bragg peaks indicate the presence of tetragonal  $\text{ZrO}_2$ . There is no evidence of a secondary phase present. Monoclinic phase peak locations are shown by vertical dashed lines, and the lack of peaks at these locations indicates that there is no crystalline monoclinic component present.

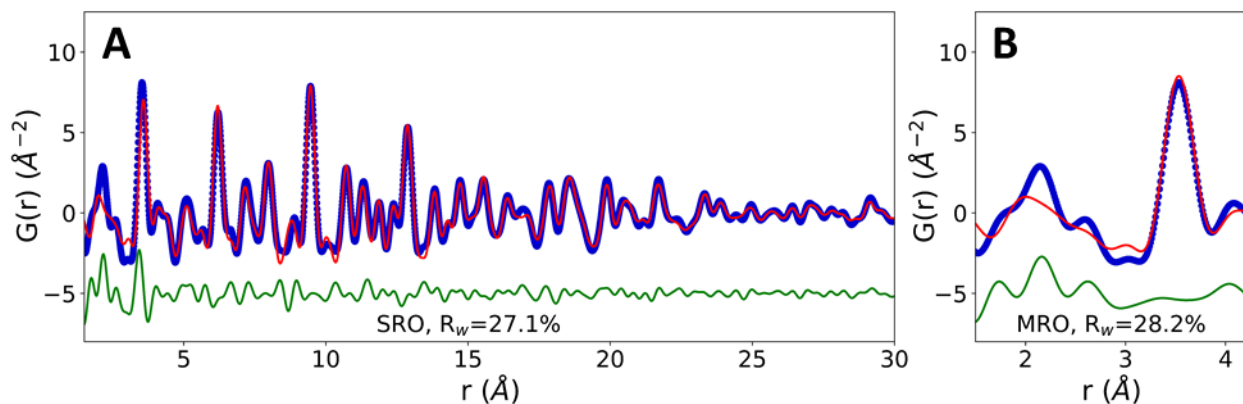


**Fig. S13 PDF refinements to oxygen interstitial tetragonal model in MWR-grown  $\text{ZrO}_2$ .** PDF data (blue) fit over an  $r$ -range of 1.5-30 Å (A) and 1.5-4.2 Å (B). Refinements to the oxygen interstitial tetragonal model are shown in red, with the difference shown below offset in green. The interstitial tetragonal model performs worse compared to both the vacancy defect model and the defect-free tetragonal phase, indicating that the addition of oxygen atoms to the tetragonal lattice does not describe the structure observed experimentally. Refinement details are given in Table S3.

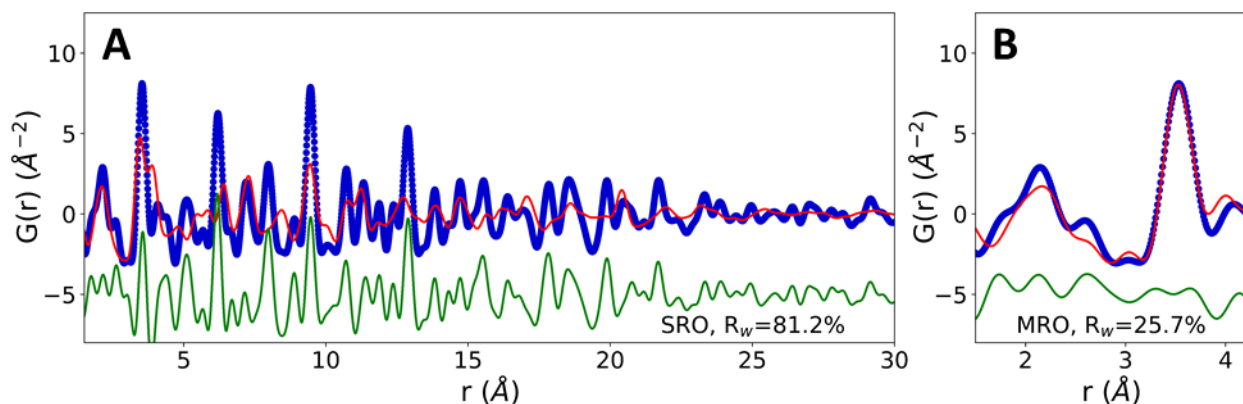


**Fig. S14 PDF refinements to oxygen interstitial monoclinic model in MWR-grown  $\text{ZrO}_2$ .** PDF data (blue) fit over an  $r$ -range of 1.5-30 Å (A) and 1.5-4.2 Å (B). Refinements to the oxygen interstitial monoclinic model are shown in red, with the difference shown below offset in green. The interstitial monoclinic model fails to represent the MRO or LRO of MWR-grown  $\text{ZrO}_2$  and yields higher  $R_w$  values than the vacancy defect model for fits the SRO. Refinement details are given in Table S3.

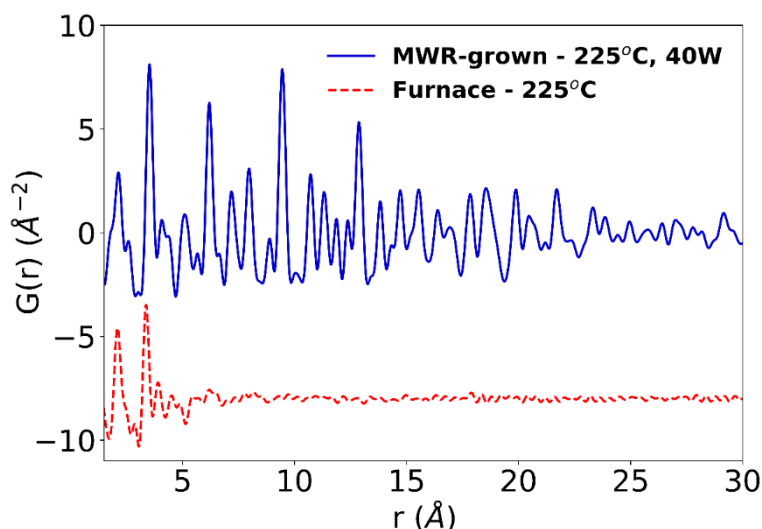


**Fig. S15 Comparison of atomic structure in furnace and MWR-grown  $\text{ZrO}_2$  at 225°C.** (a) MWR-grown  $\text{ZrO}_2$  (solid blue) displays clearly distinguished peaks in the PDF data out past 30 Å, indicating the presence of periodicity in the atomic structure. In contrast,  $\text{ZrO}_2$  grown in the furnace (dashed red) show structural coherence out to only ~5 Å, indicating a fully amorphous atomic structure.

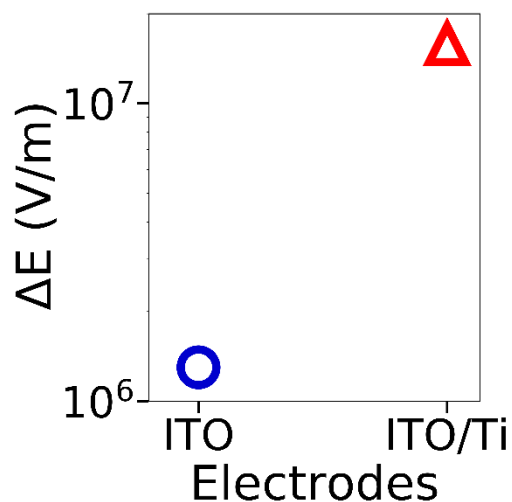


**Fig. S16 Change in electric field based on electrode material during MW-CV.** The magnitude of the electric field during MWR exposure increases by an order-of-magnitude when replacing one ITO electrode with a higher electrical conductivity Ti layer. The electric field intensity with two ITO electrodes is shown by the blue circle and the intensity with one ITO and one TI electrode is shown by the red triangle.

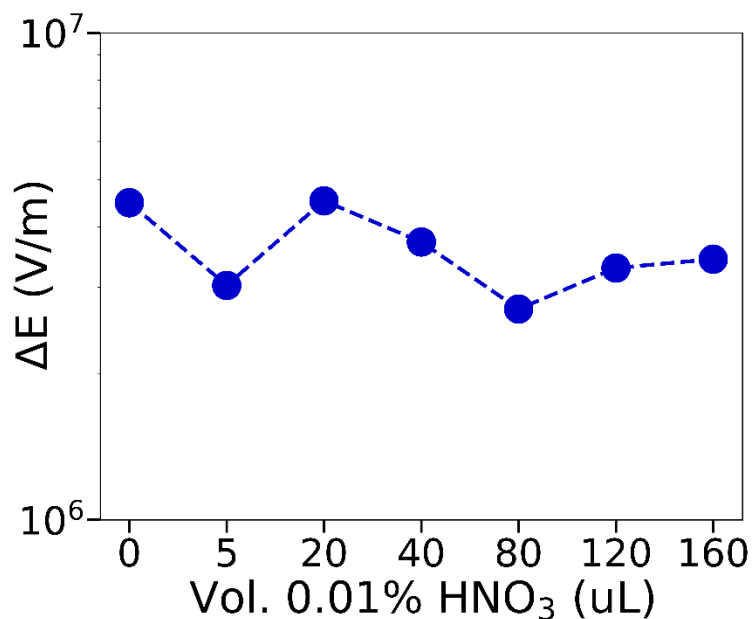


**Fig. S17 Change in electric field based on solution ion concentration during MW-CV.** The magnitude of the electric field remains constant regardless of the solution ion concentration, indicating that MWR absorption by the conducting substrate mediates the high local electric field intensity observed.

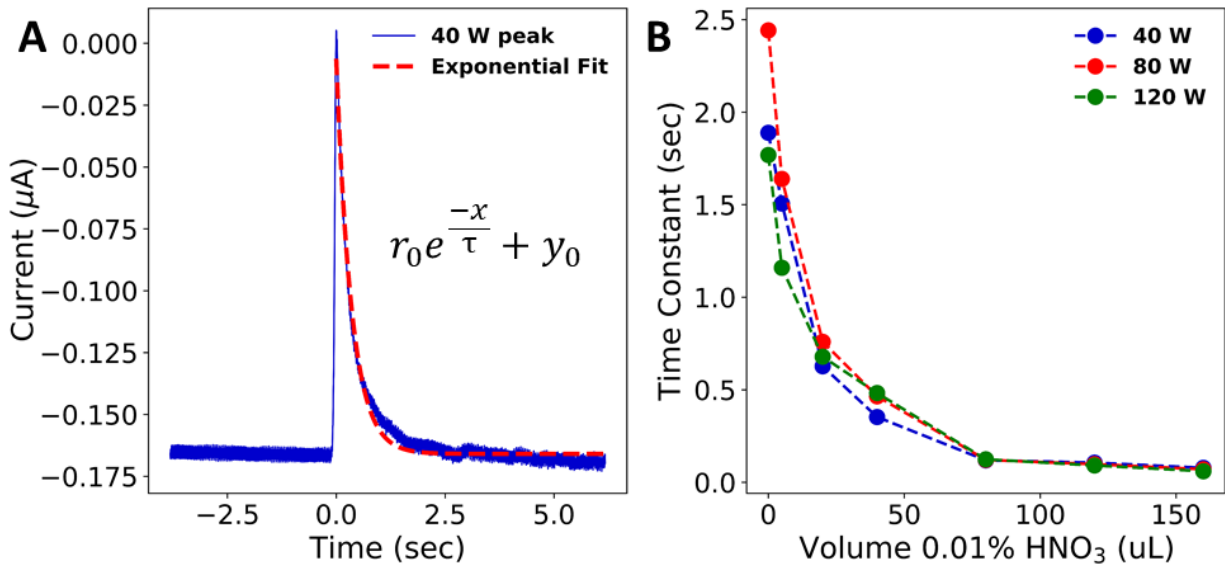


**Fig. S18 Time constants for ion movement during MW-CV.** (a) MW-CV peak from a 40 W MWR pulse using ITO electrodes, fit to a model of exponential decay. (b) Time constant,  $\tau$ , values across different MWR power levels for various  $\text{H}^+$  ion concentrations. The decrease in  $\tau$  with higher ion concentration indicates that higher ion concentrations promote faster ionic movement to the ITO surface.  $\tau$  values quickly converge across all power levels as the  $\text{H}^+$  concentration increases.

**Table S3: PDF fit parameters**

<b>A. Tetragonal ZrO<sub>2</sub> boxcar fit parameters (Fig. 3D-F) – MWR-grown 225°C, 40 W</b>			
	<b>SRO</b>	<b>MRO</b>	<b>LRO</b>
a (Å)	3.550	3.550	3.551
b (Å)	-	-	-
c (Å)	5.092	5.106	5.110
Zr U <sub>iso</sub> (Å <sup>2</sup> )	0.00805	0.00777	0.00617
O U <sub>iso</sub> (Å <sup>2</sup> )	0.00950	0.0124	0.0142
D <sub>c</sub> (Å)	26.8	67.9	56.1
δ <sub>2</sub>	-0.87	-	-
R <sub>w</sub>	24.2%	16.0%	22.8%
<b>B. Full <i>r</i>-range monoclinic, tetragonal, and cubic phase fit results (Fig. S6) - 225°C, 40 W</b>			
	<b>Monoclinic</b>	<b>Tetragonal</b>	<b>Cubic</b>
a (Å)	5.187	3.551	5.047
b (Å)	4.895	-	-
c (Å)	5.571	5.101	-
β (°)	95.85	-	-
Zr U <sub>iso</sub> (Å <sup>2</sup> )	0.0105	0.00853	0.00952
O U <sub>iso</sub> (Å <sup>2</sup> )	0.0353	0.0157	0.0521
D <sub>c</sub> (Å)	52.9	44.5	40.7
δ <sub>2</sub>	1.18	1.54	2.70
R <sub>w</sub>	74.7%	23.9%	24.8%
<b>C. 1.5-4.2 Å monoclinic, tetragonal, and defect model fit results (Fig. S10) - 225°C, 40 W</b>			
	<b>Monoclinic</b>	<b>Tetragonal</b>	<b>Defect model</b>
a (Å)	4.960	3.595	8.495
b (Å)	5.595	-	8.495
c (Å)	5.438	4.818	9.163
β (°)	97.51	-	-
Zr U <sub>iso</sub> (Å <sup>2</sup> )	0.00524	0.00927	0.00253
O U <sub>iso</sub> (Å <sup>2</sup> )	0.4066	0.0396	0.0203
δ <sub>2</sub>	4.18	2.64	2.29
R <sub>w</sub>	25.4%	25.9%	23.7%
<b>D. Defect model boxcar fit parameters (Fig. 4C-D and Fig. S12) - 225°C, 40 W</b>			
	<b>SRO</b>	<b>MRO</b>	<b>LRO</b>
a (Å)	8.770	8.818	8.803
b (Å)	8.758	8.749	8.717
c (Å)	8.734	8.664	8.711
Zr U <sub>iso</sub> (Å <sup>2</sup> )	0.00579	0.00315	0.00468
O U <sub>iso</sub> (Å <sup>2</sup> )	0.0297	0.00986	0.0103
D <sub>c</sub> (Å)	34.3	83.8	61.2
δ <sub>2</sub>	2.79	-	-
R <sub>w</sub>	22.5%	20.0%	31.5%

<b>E. Monoclinic phase boxcar fit parameters (Fig. 4C-D and Fig. S12) - 225°C, 40 W</b>			
	<b>SRO</b>	<b>MRO</b>	<b>LRO</b>
a (Å)	5.087	3.779	5.143
b (Å)	5.381	5.561	5.316
c (Å)	5.414	4.422	5.368
$\beta$ (°)	93.97	101.33	99.61
Zr $U_{iso}$ (Å <sup>2</sup> )	0.00534	0.005	0.005
O $U_{iso}$ (Å <sup>2</sup> )	0.0142	0.005	0.005
$D_c$ (Å)	94.0	40	40
$\delta_2$	1.5	-	-
$R_w$	62.2%	96.8%	97.9%

<b>F. 10-30 Å tetragonal phase fit results to MWR-grown ZrO<sub>2</sub> at various power levels (Fig. 6B)</b>			
	<b>40 W</b>	<b>80 W</b>	<b>120 W</b>
a (Å)	3.575	3.548	3.570
b (Å)	-	-	-
c (Å)	5.030	5.100	5.012
Zr $U_{iso}$ (Å <sup>2</sup> )	0.0105	0.0079	0.0109
O $U_{iso}$ (Å <sup>2</sup> )	0.0527	0.0102	0.0607
$D_c$ (Å)	50.64	56.75	48.39
$R_w$	25.3%	22.7%	32.8%

<b>G. Oxygen interstitial tetragonal phase fit results to MWR-grown ZrO<sub>2</sub> (Fig. S13)</b>			
	<b>1.5-30 Å</b>	<b>1.5-4.2 Å</b>	
a (Å)	10.043	10.085	
b (Å)	10.045	10.035	
c (Å)	10.215	9.758	
Zr $U_{iso}$ (Å <sup>2</sup> )	0.00495	0.00487	
O $U_{iso}$ (Å <sup>2</sup> )	0.00999	0.0230	
$D_c$ (Å)	47.94	-	
$\delta_2$	0.47	1.22	
$R_w$	27.1%	28.2%	

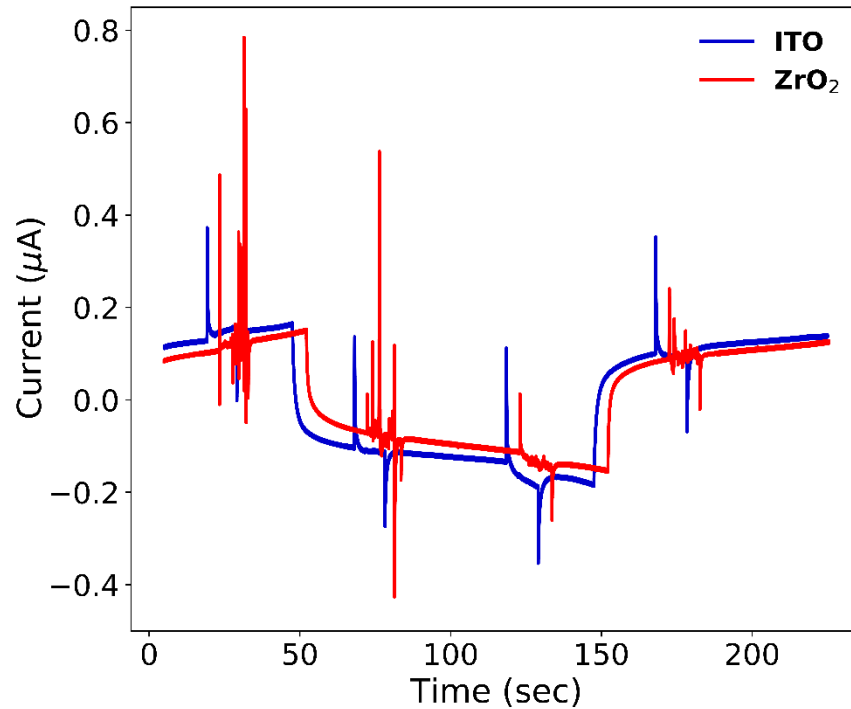
  

<b>H. Oxygen interstitial monoclinic phase fit results to MWR-grown ZrO<sub>2</sub> (Fig. S14)</b>			
	<b>1.5-30 Å</b>	<b>1.5-4.2 Å</b>	
a (Å)	10.768	9.799	
b (Å)	9.814	10.821	
c (Å)	10.821	11.131	
$\beta$ (°)	99.10	99.33	
Zr $U_{iso}$ (Å <sup>2</sup> )	0.0132	0.000820	
O $U_{iso}$ (Å <sup>2</sup> )	0.103	0.121	
$D_c$ (Å)	41.09	-	
$\delta_2$	3.06	3.35	
$R_w$	81.2%	25.7%	

**Table S4: EXAFS fit parameters for various ZrO<sub>2</sub> phases (Fig. S11) - 225°C, 40 W**

	Monoclinic	Tetragonal	Cubic	Defect model
N	1.273 ± 0.369	1.378 ± 0.311	0.696 ± 0.107	1.0489 ± 0.179
E <sub>0</sub> (eV)	0.007 ± 3.541	-7.342 ± 4.564	-7.876 ± 2.615	0.632 ± 2.763
ΔR (Å)	0.0210 ± 0.0173	0.0085 ± 0.0208	-0.129 ± 0.015	-0.0059 ± 0.0143
σ <sub>1</sub> (Å <sup>2</sup> )	0.00169 ± 0.00174	0.0061 ± 0.002	0.00615 ± 0.00170	0.00214 ± 0.00180
σ <sub>2</sub> (Å <sup>2</sup> )	0.0135 ± 0.00963	0.278 ± 2576.137	-	0.00628 ± 0.00579
σ <sub>3</sub> (Å <sup>2</sup> )	0.0269 ± 0.0288	-	-	0.0156 ± 0.0145
R <sub>w</sub>	3.5%	6.1%	6.1%	3.5%

### S3. Supplementary Figures and Tables – Conclusion



**Fig. S19 MW-CV with ZrO<sub>2</sub> surface.** MW-CV results with 40 W pulses using ITO electrodes (blue) and ITO coated with a furnace-grown ZrO<sub>2</sub> film at 225°C (red). The same phenomenon of local electric field enhancement occurs even in the presence of the ZrO<sub>2</sub> layer. The additional sharp peaks present in the ZrO<sub>2</sub> sample are attributed to surface reactions occurring between the ZrO<sub>2</sub> film and the precursor solution.